REPORT DOCUMENTATION PAGE

Form Approved
OM8 No. 0704-0188

PLEASE DO NOT RETURN YOUR FORM TO THE ABOVE ADDRESS.

1. REPORT DATE *(DD-MM-YYYY)*	2. REPORT TYPE	3. DATES COVERED *(From - To)*
01062008	Journal Article	

4. TITLE AND SUBTITLE

Application of a New Grain-Based Reconstruction Algorithm to Microtomagraphy Images for Quantitative Characterization and Flow Modeling

5a. CONTRACT NUMBER

5b. GRANT NUMBER

EAR-0207788

5c. PROGRAM ELEMENT NUMBER

6. AUTHOR(S)

Karsten E. Thompson, Clinton S. Willson, Christopher D. White, Stephanie Nyman, Janok P. Bhattacharya, Allen Reed

5d. PROJECT NUMBER

5e. TASK NUMBER

5f. WORK UNIT NUMBER

7. PERFORMING ORGANIZATION NAME(S) AND ADDRESS(ES)

Naval Research Laboratory
Marine Geoacoustics Division
Stennis Space Center, MS 39529

8. PERFORMING ORGANIZATION REPORT NUMBER

NRL/JA/7430-07-13

9. SPONSORING/MONITORING AGENCY NAME(S) AND ADDRESS(ES)

National Science Foundation
4201 Wilson Blvd.
Arlington VA 22230

10. SPONSOR/MONITOR'S ACRONYM(S)

NSF

11. SPONSOR/MONITOR'S REPORT NUMBER(S)

12. DISTRIBUTION/AVAILABILITY STATEMENT

Approved for public release; distribution is unlimited

13. SUPPLEMENTARY NOTES

SPE 95887, June 2008 SPE Journal

14. ABSTRACT

X-ray computed microtomography (XMT) is used for high-resolution, nondestructive imaging and has been applied successfully to geologic media. Despite the potential of XMT to aid in formation evaluation, currently it is used mostly as a research tool. One factor preventing more widespread application of XMT technology is limited accessibility to microtomography beamlines. Another factor is that computational tools for quantitative image analysis have not kept pace with the imaging technology itself.

In this paper, we present a new grain-based algorithm used for network generation. The algorithm differs from other approaches because it uses the granular structure of the material as a template

15. SUBJECT TERMS

16. SECURITY CLASSIFICATION OF:			17. LIMITATION OF ABSTRACT	18. NUMBER OF PAGES	19a. NAME OF RESPONSIBLE PERSON
a. REPORT	b. ABSTRACT	c. THIS PAGE			Allen Reed
Unclassified	Unclassified	Unclassified	UU	13	19b. TELEPHONE NUMBER *(Include area code)* 202-688-5473

Application of a New Grain-Based Reconstruction Algorithm to Microtomography Images for Quantitative Characterization and Flow Modeling

Karsten E. Thompson, Clinton S. Willson, and **Christopher D. White,** Louisiana State University; **Stephanie Nyman,** University of Waikato; **Janok P. Bhattacharya,** University of Houston; and **Allen H. Reed,** Naval Research Laboratory

Summary

X-ray computed microtomography (XMT) is used for high-resolution, nondestructive imaging and has been applied successfully to geologic media. Despite the potential of XMT to aid in formation evaluation, currently it is used mostly as a research tool. One factor preventing more widespread application of XMT technology is limited accessibility to microtomography beamlines. Another factor is that computational tools for quantitative image analysis have not kept pace with the imaging technology itself.

In this paper, we present a new grain-based algorithm used for network generation. The algorithm differs from other approaches because it uses the granular structure of the material as a template for creating the pore network rather than operating on the voxel set directly. With this algorithm, several advantages emerge: the algorithm is significantly faster computationally, less dependent on image resolution, and the network structure is tied to the fundamental granular structure of the material. In this paper, we present extensive validation of the algorithm using computer-generated packings. These analyses provide guidance on issues such as accuracy and voxel resolution. The algorithm is applied to two sandstone samples taken from different facies of the Frontier Formation in Wyoming, USA, and imaged using synchrotron XMT. Morphologic and flow-modeling results are presented.

Introduction

Subsurface transport processes such as oil and gas production are multiscale processes. The pore scale governs many physical and chemical interactions and is the appropriate characteristic scale for the fundamental governing equations. The continuum scale is used for most core or laboratory scale measurements (e.g., Darcy velocity, phase saturation, and bulk capillary pressure). The field scale is the relevant scale for production and reservoir simulation.

Multiscale modeling strategies aim to address these complexities by integrating the various length scales. While pore-scale modeling is an essential component of multiscale modeling, quantitative methods are not as well-developed as their continuum-scale counterparts. Hence, pore-scale modeling represents a weak link in current multiscale techniques.

The most fundamental approach for pore-scale modeling is direct solution of the equations of motion (along with other relevant conservation equations), which can be performed using a number of numerical techniques. The finite-element method is the most general approach in terms of the range of fluid and solid mechanics problems that can be addressed. Finite-difference and finite-volume methods are more widely used in the computational fluid dynamics community. The boundary element method is very well suited for low-Reynolds number flow of Newtonian fluids (including multiphase flows). Finally, the lattice-Boltzmann method has been favored in the porous-media community because it easily adapts to the complex geometries found in natural materials.

A less rigorous approach is network modeling, which gives an approximate solution to the governing equations. It requires discretization of the pore space into pores and pore throats, and transport is modeled by imposing conservation equations at the pore scale. Network modeling involves two levels of approximation. The first is the representation of the complex, continuous void space as discrete pores and throats. The second is the approximation to the fluid mechanics when solving the governing equations within the networks. The positive tradeoff for these significant simplifications is the ability to model transport over orders-of-magnitude larger characteristic scales than is possible with direct solutions of the equations of motion. Consequently, the two approaches (rigorous modeling of the conservation equations vs. network modeling) have complementary roles in the overall context of multiscale modeling. Direct methods will remain essential for studying first-principles behavior and subpore-scale processes such as diffusion boundary layers during surface reactions, while network modeling will provide the best avenue for capturing larger characteristic scales (which is necessary for modeling the pore-to-continuum-scale transition).

This research addresses one of the significant hurdles for quantitative network modeling: the use of high-resolution imaging of real materials for quantitative flow modeling. We focus in particular on XMT to obtain 3D pore-scale images, and present a new technique for direct mapping of the XMT data onto networks for quantitative modeling. This direct mapping (in contrast to the generation of statistically equivalent networks) ensures that subtle spatial correlations present in the original material are retained in the network structure.

We refer to the network-generation technique presented here as a *grain-based algorithm*, which refers to the fact that the first step in the algorithm (prior to network generation) is the characterization of the underlying granular structure in the material. The benefits to this approach are threefold. First, mapping of the granular structure is less sensitive to image resolution than, for instance, the direct mapping of a pore skeleton. Second, because the pores in a granular material are necessarily defined by their surrounding grains, a map of the grain structure is an ideal template for generating the pore network; in principle, the map of the grain structure should be essentially independent of image resolution, which means that the network structure will correlate more strongly to granular structure than to voxel size. Finally, because the number of grains is typically orders-of-magnitude smaller than the number of voxels, the grain-based algorithms are faster than equivalent voxel-based algorithms.

In this work, we use a series of computer-generated sphere packings to validate and quantify errors in the grain-based net-

This paper (SPE 95887) was first presented at the 2005 SPE Annual Technical Conference and Exhibition, Dallas, 9–12 October, and revised for publication. Original manuscript received for review 14 July 2005. Revised manuscript received 17 September 2007. Paper peer approved 8 November 2007.

TABLE 1—PARAMETERS USED TO DEFINE THE PORE NETWORK			
Variable Association	Variable Name	Variable Type	Dimension
Network	Domain dimensions	Vector	Length
Pore	Location	Vector	Length
	Void volume	Scalar	Length^3
	Maximum inscribed radius	Scalar	Length
Throat	Interconnectivity:periodicity	Scalar:vector	
	Cross-sectional area	Scalar	Length^2
	Maximum inscribed radius	Scalar	Length
	Surface area	Scalar	Length^2
	Hydraulic conductivity	Scalar	Length^3

work-generation algorithm. The algorithm is then used to perform network modeling on two different facies from a well-characterized outcrop (Gani and Bhattacharya 2003), which illustrates the potential of network modeling to be used in a multiscale framework. Few details of the grain-reconstruction algorithm (the precursor to the network-generation algorithm) are given in this paper because they can be found elsewhere (Thompson et al. 2006). It was originally developed for the analysis of marine sands (Reed et al. 2005), but is being applied to other materials. This work extends the grain-based approach to relatively low-porosity, cemented sandstones, which pose different imaging and analysis challenges than unconsolidated sands; however, the main focus of the current paper is the generation of pore network models rather than grain characterization. Although grain structure provides an initial template, ultimately the parameters in the pore network are computed directly from the voxel image. Hence (as explained next), even if the level of consolidation in a sandstone presents problems for the grain-reconstruction algorithm, the resulting pore network will still be a quantitative, one-to-one map of the pore structure.

Background

XMT. XMT provides nondestructive and noninvasive 3D images of the interior of objects by mapping the X-ray absorption through the sample. The amount of absorption depends on the chemical composition and structure of the material and the X-ray energy. XMT is based on the reconstruction of the cross-section of an object from its projection data, which is obtained by passing a series of rays through an object and measuring the attenuation of these rays using detectors placed on the downbeam side of the object. Projections are obtained by measuring the X-ray attenuation coefficients of the sample at different angles as the sample is rotated about the vertical axis. These attenuation values are represented in images as discrete elements (pixels in 2D images and voxels in 3D images). Synchrotron radiation has several advantages over traditional X-ray sources, including high flux intensity (number of photons per second); a high degree of collimation (source divergence leads to image blur); and the ability to tune the photon energy to a single energy or frequency over a wide range using an appropriate monochromator, which can be used to make element-specific measurements.

Over the last two decades, XMT has played an increasingly important role in the characterization of porous media flow and transport. Because of its nondestructive nature and increasingly high resolution, synchrotron-based XMT provides the high-quality datasets necessary to capture the 3D microstructure of the media (Liang et al. 2000a, b; Lindquist et al. 2000; Al-Raoush and Willson 2005b) and the distribution of fluids within the pore space (Seright et al. 2002; Seright et al. 2003; Al-Raoush and Willson 2005a). The ability to characterize and correlate the void space microstructure and fluid distributions provides data to improve and validate pore-scale models.

Network Modeling. Network modeling has a long history in the oil and gas industry, beginning with the landmark paper of Fatt (1956). For an extended period, network modeling techniques employed lattice-based networks, usually decorated with a distribution of pore-body and/or pore-throat sizes. These lattice-based models are valuable for qualitative studies of transport in interconnected, heterogeneous structures. However, they have not proved to be effective for quantitative modeling of real materials.

Beginning in the early 1990s, new techniques were developed for quantitative network modeling. Bryant et al. (1993b) created physically representative network models from the highly characterized Finney packing (Finney 1970). Oren and coworkers created synthetic (computer-generated) sandstones and developed a technique for extracting networks from these structures (Bakke and Øren 1997; Øren et al. 1998). Their group has continued to develop this approach and the resulting networks have been used by a number of other investigators (Patzek 2001; Lopez et al. 2003; Valvatne and Blunt 2003). Lindquist et al. (1996) worked with 3D microtomography images and computed the medial axes of the pore structure; this approach was then extended to allow for direct generation of network structures (Sok et al. 2002). Thompson and Fogler (1997) applied the techniques of Bryant et al. (1993b) to computer-generated packed beds, and Al-Raoush et al. (2003) extended this work to allow for network structures with arbitrary connectivity. Ioannidis and coworkers have used simulated annealing and other algorithms to produce networks that conform to key statistics in real materials (Talukdar et al. 2002; Liang et al. 2000; Ioannidis et al. 1997).

For the network modeling used in this work, we borrow the terminology *physically representative network models* (Bryant et al. 1993b) to describe the general class of models, and we note two important characteristics of these structures. First, this type of network is a one-to-one mapping of a specific porous material of interest, which ensures that subtle spatial correlations in the pore structure are retained. Second, the networks are described using rigorous geometric parameters, which ensures that the pore morphology is not compromised despite the need to discretize the pore space. This latter point contrasts with techniques in which the pore structure is transformed into a network of interconnected capillaries from the outset, an approach that has been shown to cause ambiguity in the subsequent modeling of flow (Balhoff and Thompson 2004).

There is no unique or correct discretization of most real pore structures (exceptions being simple structures such as cubic packings of spheres). Likewise, there is more than one approach that can be taken to describe a network model. In this work, we use the set of parameters shown in **Table 1** to describe the network structure. In addition, the network remains linked to the original data (whether it is a voxel image or a computer-generated material). This methodology ensures that additional characterization could be performed if warranted by a particular modeling algorithm. (It guarantees, in essence, that none of the original morphologic data are lost.)

The flow modeling itself is performed by imposing conservation equation(s) at each pore in the network. This results in a set of linear or nonlinear algebraic equations, depending on the physics of the process being modeled. A description of flow-modeling

algorithms is beyond the scope of the current paper, but this information can be found in many other papers on network modeling (Bryant et al. 1993b; Bakke and Øren 1997; Patzek 2001; Lopez et al. 2003; Valvatne and Blunt 2003; Thompson and Fogler 1997; Balhoff and Thompson 2004; Bryant et al. 1993a).

Network Generation From Voxel Data. Despite the advances described in the previous section, what remains surprisingly difficult is the generation of physically representative network models directly from microtomography images of real materials. The difficulty stems from the distinct differences in the form and scale of the data structures. The XMT data consist of hundreds of millions (sometimes billions) of voxels on a Cartesian grid. In contrast, the network representation of the same porous medium is likely to be described using a much smaller data set (order 10^3–10^5 pores), which are interconnected by a complex structure of flowpaths rather than aligned with any specific coordinate system. Transforming the former to the latter is a nontrivial procedure.

Most previous work in this area employs the medial axis as a basis for characterizing the pore structure. For discretized images such as those from XMT, the medial axis is obtained by thinning the original pore structure until a one-voxel-thick skeleton remains, or by computing distance transforms in the void space (to the void/solid interface) and retaining the skeleton of local maxima. Different medial-axis structures are obtained depending on the method used, the order for thinning, the type of distance transform used, and/or the rules invoked to ensure that topology is retained (Lohman 1998). Lindquist et al. (1996) used the medial axes of 3D images to compute statistical parameters associated with the void space. They later extended their algorithm, using the medial axis as a basis for obtaining pore- and throat-size distributions, which in turn were mapped onto a network structure (Lindquist et al. 2000). Specifically, the medial axis was trimmed down to the percolating fraction and nodes were then merged (by comparing the distance separating neighboring nodes to the distance to local surfaces) to define pore locations. Pore throats were found by dilating the medial axis until the dilated cylinder contacted the bounding surfaces; pore-throat geometries were then obtained by triangulating between the medial axis and voxels along the perimeter of the constriction. Sok et el. simulated immiscible displacement on networks generated by this algorithm and compared them to immiscible displacements on regular lattices having identical values for key statistical metrics (Sok et al. 2002). Mirroring what Bryant et al. (1993a) observed for single phase flow, they note that multiphase flow behavior is not reproduced correctly on statistically equivalent networks, emphasizing the need for algorithms that capture true pore morphology. Delerue et al. (1999) applied a medial-axis technique to a 3D image of a resin-impregnated soil, and then defined the pore-size distribution in the soil by measuring the maximum inscribed balls for all voxels contained on the skeleton. Mercury intrusion was simulated directly on the voxel map (rather than a network representation). Delerue and Perrier (2002) describe in detail the various computational elements used in the algorithm. Silin et al. (2003) employed a similar approach, except that the maximal inscribed ball was found for each void-phase voxel in the packing. Though computationally more intensive, this approach allows the pores to be found independently of the skeleton. They tested their algorithm using computer-generated sphere packings and a CT image of Fontainbleau sandstone. However, pore network models were not created, and a quantitative assessment of the pore locations, sizes, and connectivity was not made.

Materials and Methods

Sandstone Samples. The samples used for this application were taken from the Wall Creek Member of the Cretaceous Frontier Formation, Wyoming, USA as part of an integrated geologic, geophysical, and engineering study (Gani and Bhattacharya 2003). Ten wellbores were drilled through the Wall Creek Member and sample plugs were selected.

Sample A is from a tidally-reworked sandstone facies within a delta front sandstone body. The permeability of this sample is severely reduced by calcite concretions. Concretions locally reduce the permeability by several orders of magnitude in approximately 15 volume % of the tidal sandstone facies (Lee et al. 2007). The sediments preserved in these rocks were derived from uplifts to the north and west. Lee et al. (2007) report that the average composition is approximately 51% quartz, 21% rock fragments, and 28% feldspars, with calcite as the dominant diagenetic cement. Feldspar and volcanic components have been highly altered by diagenesis. In uncemented rocks of the tidal sandstone facies, porosity averages approximately 0.22 and permeability is in the range of tens to a few hundred millidarcies, with a mean of 110–140 md (higher for fluvial-dominated deposits of the delta front).

Sample B is from a channel sandstone facies within the same delta front sandstone body as sample A. The provenance of this sample is thus similar to Sample A, except for calcite cement replacing some of the pore space. This sample is interpreted to be from a relatively mud-free cross-stratified channel sandstone facies. Depositional considerations would imply very high reservoir quality. The grain size is on average larger, and sorting is better than sample A. However, it is from a cemented region within the sandstone, and its reservoir quality is therefore relatively low. The greater abundance of calcite concretions in some channel sandstones is inferred to be related to the abundance of mud chips (or shale clasts). Although mud chips would decrease initial permeability, their inhibiting effect on concretion formation actually results in higher, post-diagenetic reservoir quality for channel sandstones with mud chips (Lee et al. 2007).

XMT of the Sandstone. Small samples of the sandstones were impregnated with an epoxy resin under vacuum and then cored to a length of 25 mm and a diameter of 5 mm. 5-mm-long sections of the cores were imaged at 33.07 keV energy at the 13-BMD tomography beamline, operated by GeoSoilEnviroCARS (GSECARS) at the Advanced Photon Source. Image reconstruction was performed using algorithms developed by GSECARS to convert CT attenuation data to 3D volumetric data The resultant 3D gray-scale images have a voxel resolution of 7.63 microns. Segmentation, the process of converting a gray-scale image to a 1-bit or binary image by separating the images into two populations based on gray-scale values, was performed using the indicator kriging technique (Oh and Lindquist 1999) that is part of the 3DMA software package. In this work, the pore voxels are assigned a value of 0 and the grain voxels are assigned a value of 1. **Fig. 1** contains images of the binary volume files.

The combination of mineralogy (i.e., higher absorbing elements) and X-ray energy created a relatively high signal-to-noise ratio. This less-than-ideal image quality made it difficult to completely resolve the solid and void phases and to remove the ring artifacts. Since the time that these experiments were performed, these issues have been addressed, which means that images from current experiments are generally free from these problems.

Network Construction

Overview. The input for the algorithm is a binary volume file describing the porous material of interest: voxel labels indicate whether the voxel is contained in the void phase or solid phase of the material. The algorithm operates by identifying grains, searching for pores based on the grain locations, and then creating the interconnected network using a novel restricted-burn algorithm. The significant differences between this algorithm and other network generation techniques include the following:

1. The first step in the algorithm is the identification of the granular structure, a process that is less sensitive to image resolution than techniques such as skeletonization. Consequently, networks created for the same material at two different image resolutions have very similar structure and properties.

2. The algorithm uses the granular structure as a template to help define pores. This means that the computationally expensive search for pores becomes linked to the number of grains in the image rather than the number of voxels, and the computational penalty for increasing image resolution is less severe than with other algorithms.

Fig. 1—Binary volume files for two sandstone samples: (a) tidally-reworked sandstone facies; (b) channel-sandstone facies.

3. Because the grain locations provide the framework for determining pore structure, the algorithm operates without ever computing a skeleton of the pore space. By eliminating this step, a number of problematic issues such as nonuniqueness, dependence on image resolution, and the formation of internal loops are avoided.

4. A key intermediate step between the original binary map and the final network structure assigns an integer label to every voxel (both void and solid phase) to mark the grain or the pore to which that voxel belongs. The reason for emphasizing this intermediate step is that it makes obtaining statistical information and constructing the network straightforward and unambiguous.

Grain Reconstruction Algorithm. ***Step 1. Dual-Phase Burn.*** A simultaneous grain-phase and void-phase burn is performed (using the terminology of Lindquist et al. 1996). Voxels in the solid phase are labeled with positive integers denoting the burn level and voxels in the void phase are labeled with the negative of the burn level. This convention is not necessary if the burn map remains coupled with the binary material array; however, the use of opposing signs allows the burn numbers to be written over the initial material array without losing the phase information.

Step 2. Location of Extrema. A search is performed to find local maxima in the burn assignments. These local extrema are islands of one or more voxels that are surrounded by voxels with lower burn numbers. In the simplest form of the algorithm, the local maxima are taken to be the grain centers. However, refining the grain locations using optimization leads to better results (Thompson et al. 2006). Simultaneously, the local minima can be found (which according to the sign convention are in the void phase). In practice, this step is skipped to reduce computation time because the void-phase extrema are not used to define the pore structure. However, the minima are found and reported for completeness in this paper.

Step 3. Tessellation of the Grain Centers. A periodic Delaunay tessellation is performed using the locations of the grain centers (Thompson 2002). The purpose of the tessellation is to identify likely pore locations based on the granular structure. The role of the tessellation is somewhat subtle, and the following points are worth clarifying:

1. In contrast to other techniques where the Delaunay tesselation is used to define pore structure (Bryant et al. 1993b; Thompson and Fogler 1997; Al-Raoush et al. 2003; Bryant et al. 1993a), it does not influence the structure of the pores in the current algorithm. In fact, the only restriction that it imposes is on the total number of pores: the algorithm will not find more pores than the number of tetrahedrons in the tessellation. This limitation should not be of practical consequence because the tendency of the Delaunay tessellation is to identify too many pores [by splitting single pores into multiple tetrahedrons; see Al-Raoush et al. (2003)]. Furthermore, this restriction can be relaxed if necessary at the expense of increased computation time (see Item 3).

2. Use of the Delaunay tessellation to aid in the identification of pore locations provides an advantage over erosion/dilation techniques because the number of pores that are located for a given porous medium is relatively insensitive to voxel resolution. This issue is demonstrated later in the validation section.

3. Finally, the tessellation is a valuable but not essential part of the algorithm. An alternative approach would be to perform the optimizations described in the next step beginning with every void-phase voxel. However, even for the relatively small sandstone datasets used here, this approach requires solving ~5,000,000 nonlinear optimization problems (in contrast to ~25,000 optimizations when the tessellation is used as a template).

Step 4. Locating Pores. In the Introduction, we note that the division of void space into pores is somewhat arbitrary. In this work, we use the distance function $d(x,y,z)$, whose value gives the minimum distance from the point $[x,y,z]$ in the void space to a grain surface (Luchnikov et al. 1999), and then define a pore as any local maxima in d. In practice, this definition corresponds to an accepted definition for pores: locations of maximum-diameter spheres that can be inscribed into the void space, and that are constrained from movement by the surrounding solid phase (Scheidegger 1974). In Step 4, these maximum-diameter inscribed spheres are located by performing repeated optimization procedures (to maximize d) using the tetrahedrons as seed locations to start the optimizations.

The optimizations themselves are performed using a modified Powell's method (Press et al. 1992), which is a direction set method effective for situations where gradients in the objective function cannot be calculated directly. In essence, the procedure repeatedly performs 1D line minimizations. Various schemes are available to choose the minimization directions, most based on estimating new conjugate directions from the history of the optimization.

As each extremum is found, the voxel containing its x,y,z location is marked with the pore number. If a different seed has already converged to this same voxel (though the coordinate location would rarely be exactly the same), a new pore is not added to the list. Hence, Step 4 ends having generated a list of N pore locations and inscribed radii (i.e., maximum d values) along with N void-phase voxels labeled with the corresponding pore number. At this point, the pores are no longer tied to their seed

tetrahedrons and there is no further need for the Delaunay tessellation in the algorithm.

Step 5. Pore Merging. A viable option is to use all pore locations identified in Step 4, and proceed with constructing the network. However, in real cases, many pores overlap with one another by a significant amount, the overlaps being caused by one of two reasons: (a) the local pore geometry causes two independent extrema to be in proximity; (b) two different seeds have led to the same extremum, but numerical error or optimization tolerances have caused the computed extrema locations to differ by at least one voxel.

In either of these cases, there is good reason to merge two largely overlapping pores into one. Various merge criteria can be devised. In the current algorithm, pores are merged only if one inscribed sphere encompasses the center of a neighboring inscribed sphere. The location and radius of the larger inscribed sphere is used as a seed, and a local optimization is performed once again to verify the location of the merged pore. With the adjusted pore locations (owing to the reoptimization of merged pores), we have found it advisable to make another pass to check whether additional pores should be merged, and indeed to continue this merge→re-optimization procedure iteratively until no more pores are merged. Step 5 ends with the same information as Step 4 (pore locations, radii, and corresponding voxel assignments), but with fewer and more spatially independent pores.

Step 6. Grain and Pore Assembly. Step 6 is the key intermediate step mentioned in the previous overview: the assignment of all voxels in the image to one of the grains or pores identified in Steps 2 or 5, respectively. This step is performed using a novel restricted burn algorithm, which is described in more detail in the context of grain reconstruction elsewhere (Thompson et al. 2006). In short, it assembles a cluster of voxels together that are tied to one of the grain or pore locations respectively, in accordance with the local geometry.

A summary of the logic for this restricted burn procedure (Step 6) is the following:

1. Set the minimum burn level to the largest (absolute) value found in the pore space.
2. Loop through all voxels in the domain.
3. If the current voxel borders a voxel already assigned to a particular pore and its absolute burn level is greater than or equal to the current minimum burn level, assign it to the same pore as the assigned neighbor.
4. If any new voxels were assigned during the last pass, go to Step 2.
5. If no new voxels were assigned during the last pass, reduce the minimum burn level by 1; go to Step 2.

Step 7. Pore Morphology and Network Construction. Once Step 6 is complete, determining morphologic parameters and constructing the network is a straightforward process. The total volume of each pore is obtained by summing the volume of all voxels assigned to that particular pore. The inscribed pore radii are already known from the Step 4 and Step 5 computations.

In our definition of network structure, pore throats have no volume but rather are defined by the faces where two pore-elements come into contact. Hence, the pore-throats, like the pores, have rigorous geometric parameters associated with them. The unit normal for the pore-throat interface is found by averaging the orientation of all voxel interfaces associated with the given throat. The total cross-sectional area of the throat is then found by summing the areas of voxel faces at this interface projected onto this local unit normal. Use of the projected area prevents overestimating the area because of the staircase-like surface created by the voxels. The inscribed area of the throat is found by determining the largest inscribed sphere whose center is located on the throat interface.

Grain surface area is also assigned as a throat parameter because it affects permeability as well as phenomena such as absorption and chemical reactions on grain surfaces. The surface area is assigned by estimating the surface area for each surface voxel, and then assigning that element of surface to its closest throat. This approach ensures that the surface area is conservative (i.e., the sum of all pore throat surface areas equals the total surface area in the packing), thus providing a good theoretical foundation for its use in modeling.

The last parameter that should be mentioned is the pore-throat hydraulic conductance of each throat, which is necessary for computing permeability and performing dynamic flow simulations. In general, the conductance is computed using some combination of the previously mentioned parameters, through generation of an equivalent capillary. In this work, we use essentially the same approach used in Thompson and Fogler (1997) (without the FEM computations). Further work includes evaluating the best way to compute throat conductivities for various types of materials.

The network itself is defined by mapping out the connectivity of each pore, which is defined by the list of neighboring pores that share voxel-voxel contacts. There are no limitations on the structure of the networks thus obtained (i.e., coordination numbers, etc.), and the resulting network files have exactly the same format as network descriptions from computer-generated media (Balhoff and Thompson 2004). Once the network is constructed, plots of pore-size distribution, throat-size distribution, and coordination number can be made directly from the data in the network file, without having to return to the large voxelized data sets.

Validation. The grain-reconstruction algorithm has been tested extensively using computer-generated packings of spheres and cylinders as well as XMT data from unconsolidated particles and sands. Separately, the network-generation algorithm has been tested using a series of computer-generated packings of spheres. This approach is valuable for three reasons: First, the pore structure in the material is known exactly; hence, the validity of the network generation process can be assessed in a quantitative manner. Second, the computer-generated structures can be discretized at arbitrary voxel resolution, which provides good benchmarks for the accuracy that can be expected with data from real materials. Third, the computer-generated data are free from noise and artifacts, which allows validation to be focused solely on the network construction (rather than imaging and segmentation issues).

Three sphere packings were used for validation: a cubic packing, a rhombohedral packing, and a random packing. The two regular packings span the full range of attainable porosities for monodisperse spheres and the pore structure is known exactly. The random packing is more representative of real materials. No single network is correct for the random case. However, the modified Delaunay Tessellation (MDT) algorithm (Al-Raoush et al. 2003) is a fairly rigorous method for extracting the pore structure and can be used for comparison to the networks generated from the voxelized images.

Table 2 explains the notation used for reporting the statistical results. Selected quantitative data are presented in **Table 3**. (Data for the computer generated packings are in units of sphere diameters; data for the sandstone shown later are in microns.) Note that for the three sphere packings, the top row of each section contains parameters obtained from the MDT networks. These parameters quantify the error in the voxel-based networks. For the cubic and rhombohedral packings, the MDT values agree with theoretical values from a unit-cell analysis and are exact within the numerical tolerances set in the MDT algorithm. As mentioned previously, there are no "correct" morphologic values for the random packing. However, the MDT algorithm is an excellent benchmark because it is based on Delaunay analysis (Finney 1970; Mellor 1989) and allows for variable pore connectivities (which are not possible with the unmodified Delaunay tesselation).

Identification of Pores. Column $\#EV$ is the number of extrema in the void-phase burn. This parameter is the most logical choice for determining pore locations if the burn information were to be used directly. However, notice the very strong dependence of these values on image resolution (at least for the noncubic structures). For the rhombohedral packing, the number of void-phase extrema varies from four to 328 as image resolution is increased over an order-of-magnitude range (the true number of pores is 192). For the random packing, number of burn extrema varies between 63 and 803 as resolution varies from 10 VPD to 125 VPD (the best

TABLE 2—EXPLANATION OF PARAMETERS USED IN TABLES

Parameter	Description
A_{cs}	Cross sectional area of a pore throat (ave)
A_s	Surface area assigned to a pore throat (ave)
D_G	Grain diameter (ave)
D_P	Pore diameter (inscribed) (ave)
D_{PT}	Pore-throat diameter (inscribed) (ave)
# *EG*	Number of extrema in the grain-phase burn
# *EV*	Number of extrema in the void-phase burn
K	Permeability (subscripts indicate flow direction)
L_{PT}	Length of pore throat (ave)
MBG	Maximum burn number in the grain phase
MBV	Maximum (absolute) burn number in the void phase
N_G	Number of grains
N_P	Number of pores
PLE	Average error (%) in the computed pore locations
# P_I	Number of pores initially found from the tetrahedron seeds
# *PM*	Number of one-to-one pore matches (reconstructed packing vs. original)
# P_M	Final number of pores after the iterative merging/reoptimization process
# *Tet*	Number of tetrahedrons used as seeds for pore locations
$V_{F,min}$	Minimum number of voxel faces required for a pore throat to be formed
# *Vox*	Number of voxels in the data set
V_p	Volume of a pore (ave)
VPD	Voxels per particle diameter
VR	Voxel resolution
Z	Pore coordination number
ε	Porosity
Other	
ave	Arithmetic average
Sd	Standard deviation

estimates for number of pores in this packing are ~400). Clearly, the void-phase burn provides a poor indicator of pore location, which is related to the problems with skeletonization that were mentioned previously.

In the current algorithm, the grain structure is used as a template for determining pore locations. The initial seeds for pore locations are based on a Delaunay tessellation of the grain locations. Table 3 lists the number of Delaunay tetrahedrons (see column #*Tet*). The number of largest-inscribed-spheres obtained from these seeds is listed in column #P_I. Note that the numbers in both of these columns are relatively insensitive to image resolution since they are tied to the grain structure rather than the voxel structure.

The cubic packing has significantly fewer inscribed spheres (i.e., pores) than tetrahedron seeds. The reason for this difference is that assembling a cubic pore requires at least five tetrahedrons. If the optimization routine were exact, all five seeds would converge on the same central pore location. In reality, more than one seed will usually converge on the same central voxel, and is listed only once. The fact that #P_I decreases with increasing resolution is somewhat counterintuitive (because higher resolutions provide many more voxels in which the optimizations can land). However, the reason for this effect is the increased accuracy of the optimization procedure as resolution increases (which is a consequence of more precise distance-to-surface calculations).

The more important value is the final number of pores after merging (#P_M). For the cubic packing, this value is exact for all resolutions. For the rhombohedral packing, it is exact for resolutions of 16.7 VPD and above. For the random packing, an exact number of pores can never be defined unequivocally. However, the values obtained from the current algorithm and the MDT algorithm agree reasonably well. Results from the random packing also illustrate the efficiency of the grain-based approach. Examining the number of tetrahedrons (each of which generates a seed point to search for a pore) shows that ~620 nonlinear optimization procedures were performed to find the initial pore locations, independent of image resolution. In contrast, ~32 million of these same computations would have been required for the 100 VPD image if each void-phase voxel were tested to find its maximum inscribed sphere.

Accuracy of Pore Locations and Sizes. The pore location is defined as the center of the largest sphere that can be inscribed into a given void space. For the cubic packing, the results are essentially exact in cases where an integer VPD value is used. For noninteger VPD values, the voxels cannot be divided evenly between pores in the packing. Consequently, there remain slight distributions in pore parameters, even at high VPD values. However, error remains fairly low in key parameters such as pore volume (see V_P) and pore location (Table 3, column PLE). The rhombohedral packing is a much more rigorous test because the pores are not symmetric with respect to the Cartesian voxel grid and also because they are small. The error in pore locations is significant at low resolutions (where pore dimensions can be as small as a single voxel), but it appears to decrease monotonically with increasing voxel resolution.

The accuracy for the random packing network is somewhat harder to assess, mostly because the number of pores found does not agree exactly for the MDT vs. voxel-based networks. Column #*PM* in Table 3 provides statistics for the fraction of pores with a one-to-one match with the MDT network (defined when the center of one and only one pore from the voxel network lies inside an inscribed pore of the MDT network). Also shown is the average error in pore location for these one-to-one matches.

Pore parameters are computed with increasing accuracy as the voxel resolution increases. This trend is easy to confirm by examining the results for the cubic packing. The same trend occurs for the other two packings, but is harder to assess from simple statistics: a rhombohedral packing contains two distinct types of pores (which is why the standard deviation remains non-zero for both the MDT results and the high-VPD results) and the random packing has a distribution of pores.

Coordination Number. Determining the pore coordination number (the number of throats emanating from a pore and connecting to other pores) remains the biggest problem for this algorithm (as well as other network generation algorithms). For the cubic packing, the coordination number is exact for integer VPD values, again because of the fact that pore boundaries are coincident with voxel boundaries. For resolutions that produce noninteger VPD values, the average coordination numbers are slightly higher and the maximum coordination numbers are significantly higher than they should be. The problem is illustrated in **Fig. 2**, which shows two pores assembled from a cubic packing with a noninteger resolution of 21.3 VPD. Although they are constructed correctly (within the limitations of the voxel resolution), the fact that the pore boundaries are not coincident with voxel boundaries creates a contact between two voxel faces at a position that should be a corner-corner contact in reality (and therefore should not register as a throat connection). The numbers from the noninteger VPD cases indicate that this problem occurs less often than once per pore on average (though certain pores are assigned many extra neighbors, as evidenced by the high values for the maximum coordination numbers). For the rhombohedral packing, the problem is similar, though no resolution generates the exact coordination pattern because the rhombohedral pore boundaries never lie along voxel boundaries.

For random pore structures, the problem is exacerbated. The pore geometries are more irregular (anomalies are not limited to corner-corner contacts as with the cubic packing) and, like the rhombohedral packing, the Cartesian voxel system does not allow

TABLE 3—RESULTS FOR THE SPHERE PACKINGS: REGULAR AND DISORDERED

Image Resolution			Burn Parameters				Pore Parameters									Pore-Throat Parameters									
VR	*VPD*	*# Vox*	*MBG*	*MBV*	*# EG*	*# EV*	*# Tet*	*# P_i*	*# P_M*	D_P		V_P		*# PM*	*PLE*	*Z*			D_{PT}		A_{CS}		A_S	
										ave	sd	ave	sd		(%)	min	max	ave	ave	sd	ave	sd	ave	sd
Cubic Packing																									
MDT									**64**	**0.7317**	**0**	**0.4764**	**0**			6	6	6	**0.4142**	**0**	**0.5227**	**0**	**1.0472**	**0**
0.100	10.0	40×40×40	3	2	64	64	458	215	64	0.6996	0.0003	0.4480	0	64/64	0.07	6	6	6	0.3772	0	0.5046	0	0.9037	0.0367
0.096	10.3	41×41×41	3	3	64	64	443	201	64	0.7141	0.0308	0.4512	0.0526	64/64	6.93	6	13	6.94	0.3960	0.0886	0.4506	0.1416	0.7334	0.2049
0.090	11.0	44×44×44	4	2	64	64	458	218	64	0.7190	0.0104	0.4583	0.0248	64/64	0.09	6	6	6	0.4650	0.0454	0.5097	0.0221	0.8442	0.0443
0.080	12.5	50×50×50	4	3	64	64	459	139	64	0.7190	0.0302	0.4788	0.0120	64/64	0.08	6	6	6	0.4519	0.0260	0.5357	0.0157	0.9087	0.0345
0.050	20.0	80×80×80	6	4	64	64	458	270	64	0.7428	0.0000	0.4720	0	64/64	0.06	6	6	6	0.4078	0	0.5171	0	0.9247	0.0404
0.047	21.3	85×85×85	7	5	64	64	418	157	64	0.7189	0.0119	0.4742	0.0082	64/64	2.37	6	12	6.66	0.3856	0.0978	0.4766	0.1399	0.8594	0.2069
0.020	50.0	200×200×200	14	11	64	64	458	187	64	0.7366	0.0001	0.4740	0	64/64	0.05	6	6	6	0.4184	0	0.5166	0	0.9920	0.0164
0.010	100.0	400×400×400	29	21	64	64	458	194	64	0.7261	0.0000	0.4760	0	64/64	0.05	6	6	6	0.4198	0	0.5220	0	1.0093	0.0095
Rhombohedral Packing																									
MDT									**192**	**0.2878**	**0.0892**	**0.0612**	**0.0498**			4	8	5.33	**0.1547**	**0**	**0.2266**	**0**	**0.3927**	**0.0585**
0.100	10.0	40×34×32	3	2	64	4	384	277	177	0.3374	0.0503	0.0607	0.0365	167/192	41.40	2	20	6.71	0.2310	0.0437	0.1761	0.0457	0.2232	0.0603
0.060	16.7	66×57×54	5	2	64	160	384	261	192	0.2994	0.0742	0.0599	0.0472	192/192	23.02	1	20	6.38	0.1795	0.0205	0.1827	0.0410	0.2688	0.0792
0.040	25.0	100×88×81	8	4	64	88	384	271	192	0.2922	0.0786	0.0598	0.0470	192/192	18.04	2	19	6.41	0.1489	0.0309	0.1862	0.0560	0.2785	0.0976
0.020	50.0	200×173×163	15	6	64	192	384	320	192	0.2875	0.0836	0.0608	0.0491	192/192	6.80	1	26	6.60	0.1339	0.0421	0.1877	0.0705	0.2958	0.1080
0.015	66.7	226×230×217	20	9	64	251	384	295	192	0.2863	0.0846	0.0607	0.0493	192/192	6.38	1	30	6.25	0.1266	0.0500	0.1788	0.0808	0.2863	0.1161
0.010	100.0	400×346×326	29	13	64	328	384	276	192	0.2901	0.0999	0.0605	0.0493	192/192	4.14	1	31	6.10	0.1301	0.0505	0.1885	0.0785	0.3057	0.1094
Random Sphere Packing																									
MDT									**409**	**.3591**	**0.0921**	**0.0784**	**0.0782**			3	**12**	**4.6**	**0.2631**	**0.0857**	**0.3541**	**0.0940**	**0.3350**	**0.1220**
0.100	10.0	43×43×43	3	3	100	63	615	489	301	.3975	0.0946	0.1063	0.1069	271/409	40.47	2	20	6.71	0.2900	0.0767	0.2620	0.1214	0.2471	0.1296
0.050	20.0	87×87×87	6	6	100	127	619	562	346	.3559	0.0930	0.0926	0.1005	311/409	26.79	1	20	6.38	0.2334	0.0900	0.2649	0.1351	0.2563	0.1386
0.040	25.0	109×109×109	8	7	100	155	619	581	369	.3461	0.0968	0.0868	0.1059	310/409	23.46	2	19	6.41	0.2231	0.0921	0.2566	0.1380	0.2441	0.1428
0.025	40.0	175×175×175	12	11	100	278	620	599	376	.3402	0.0942	0.0853	0.1088	322/409	23.40	1	26	6.60	0.2083	0.1015	0.2484	0.1479	0.2392	0.1448
0.010	100.0	438×438×438	29	27	100	670	619	611	401	.3309	0.0977	0.0800	0.1331	334/409	21.44	1	30	6.25	0.1937	0.1100	0.2240	0.1583	0.2424	0.1518
0.008	125.0	548×548×548	37	34	100	803	619	612	407	.3334	0.0959	0.0788	0.1312	350/409	22.90	1	31	6.10	0.1948	0.1142	0.2185	0.1643	0.2455	0.1527

Fig. 2—Non-physical pore-throat connection in a cubic packing of spheres.

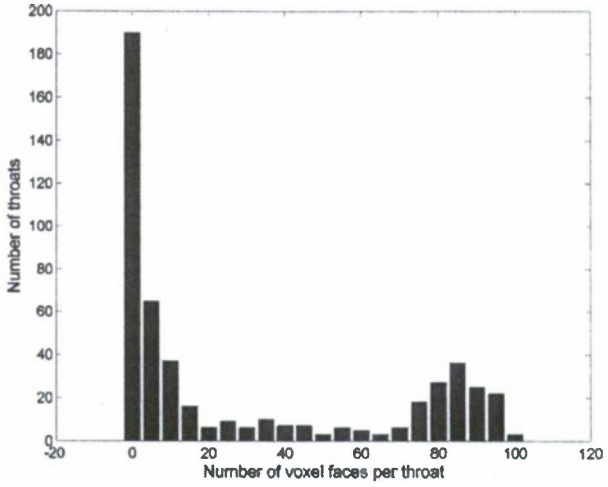

Fig. 3—Histogram of the number of voxel-voxel contacts in pore throats in a random packing of spheres.

for perfect breaks in the pore geometry. Estimates of average pore coordination number fall into the mid-sixes range. These values are probably too high, again because of identification of voxel-voxel connections that should not register as pore-pore connections (a fact also evidenced by the large values of maximum coordination number).

The obvious solution to this problem is to set a minimum limit for the number of voxel-voxel contacts that constitutes a pore throat. For the cubic packing, requiring pore throats to be composed of three or more voxel faces led to perfect coordination numbers at all non-integer resolutions tested. For the 40 VPD random packing, **Fig.** 3 shows a histogram of the number of voxel faces found at a throat connection. The histogram has a broad minimum before the population begins to increase at around 70 voxel-faces per throat. Interestingly, the theoretical minimum for throat size at this resolution is 64 voxel-faces per throat, which lends credence to the histogram. These two factors suggest that connections made at less-than ~64 voxel-faces/throat are anomalies and should be discarded. **Table 4** shows the results for various minimum-voxel limits applied to the 40 VPD random sphere packing. For a conservative minimum of 50 voxel-faces/throat, the revised throat parameters are in much better agreement with the MDT values, with the average pore coordination number reduced to 4.67. A more aggressive limit of 63 voxel-faces per throat caused the other parameters to deteriorate, indicating that real throats are being discarded with this higher limit.

Unfortunately, it is difficult to generalize an effective rule for how to limit interconnectivity. Creating a histogram (e.g., Fig. 3) on a case-by-case basis is a sensible and fairly easy approach with an automated algorithm. However, tomographic data from real materials that we have tested do not show the bimodal distribution found in Fig. 3 and therefore do not provide a strong rationale for a cutoff value. We suggest the following approach. For the purposes of network generation, small values or no cutoff should be used because extra throats will have negligible effect on most transport processes (because of their very small size), and because one risks eliminating what the tomography has identified as "real" connections. For the purposes of statistical analysis, the extra throats do cause a problem because they affect the calculation of coordination number and average throat parameters. In these cases, it is worth the extra effort to assess the distribution of voxel contacts, and provide a cutoff if a case can be made to do so. Finally, the use of geometric averages should improve the statistical characterization even in cases where small throats are mistakenly identified.

Results

Networks were created using the sample A and sample B sandstone images. For illustration purposes, ball-and-stick depictions of the network structures are shown in **Fig. 4.** Comparing these networks to the Fig. 1 tomography images emphasizes the one-to-

TABLE 4—CHANGES IN PORE-THROAT PARAMETERS BY LIMITING CONNECTIVITY

	Pore-Throat Parameters								
	Z			D_{PT}		A_{CS}		A_S	
VF_{min}	min	max	ave	ave	sd	ave	sd	ave	sd
MDT	2	12	4.60	0.2627	0.0846	0.3548	0.0963	0.3369	0.1233
0	1	26	6.60	0.2083	0.1015	0.2484	0.1479	0.2392	0.1448
1	1	26	6.60	0.2083	0.1015	0.2484	0.1479	0.2392	0.1448
2	1	23	6.08	0.2215	0.0950	0.2673	0.1386	0.2607	0.1475
3	1	21	5.87	0.2269	0.0921	0.2757	0.1338	0.2697	0.1477
4	1	20	5.71	0.2310	0.0898	0.2820	0.1299	0.2770	0.1472
5	1	20	5.71	0.2310	0.0898	0.2820	0.1299	0.2770	0.1472
10	1	19	5.24	0.2422	0.0842	0.3019	0.1164	0.3018	0.1414
50	1	18	4.67	0.2523	0.0814	0.3251	0.1008	0.3386	0.1255
63	0	17	4.57	0.3113	0.0960	0.2981	0.1536	0.3108	0.1792

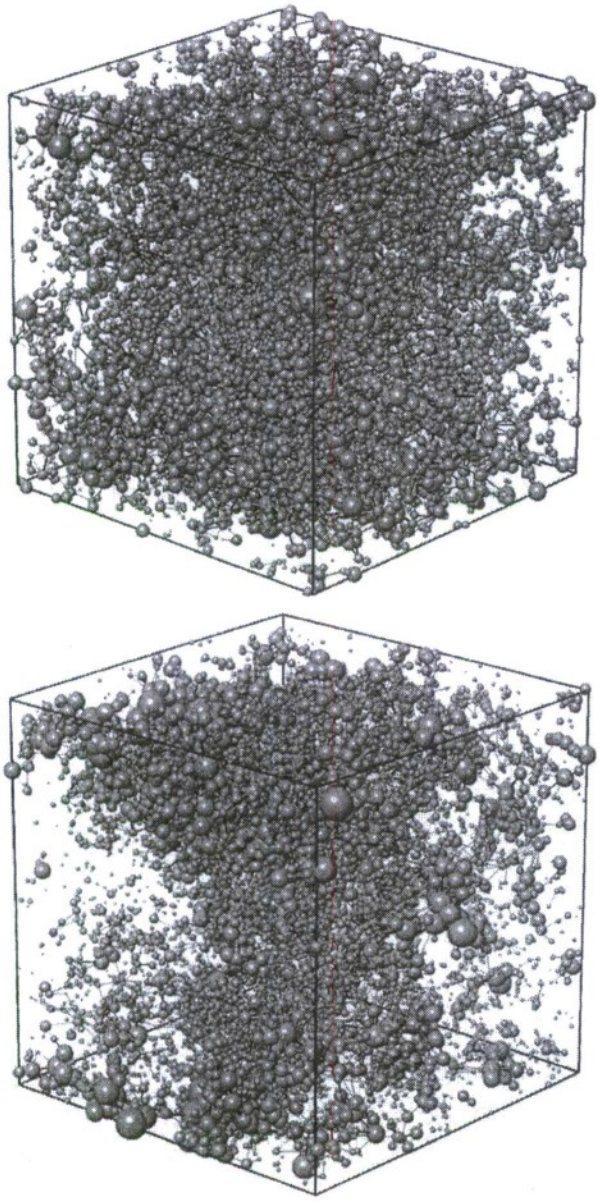

Fig. 4—Ball-and-stick schematic illustration of network models corresponding to the two different sandstone samples.

one mapping that is achieved using a physically representative network modeling technique.

For the sample A data set, two different network reconstructions have been performed. The first uses the grain-reconstruction algorithm. For comparison, a second run was performed in which the search for pores was performed directly on the void-phase voxels, without use of the grain reconstruction and the Delaunay tessellation.

All runs were performed on IBM Power5 8-way 1.90GHz p575 machines, which are operated by LSU's high-performance computing center. The grain-based algorithm required ~1 hr of run time, while the voxel based network required ~24 hrs to run.

Morphologic Parameters. **Fig. 5** contains an image of the grain reconstruction process for sample A, which is included for general interest. Shading is assigned randomly to grain numbers to give a visual indication of the discretization into individual grains. (The missing piece at the bottom left corner is an artifact caused by the graphics software.)

In previous tests of the algorithm on tomography images of unconsolidated sands, two problems with the grain-reconstruction

Fig. 5—Grain reconstruction of the sandstone sample A.

process were identified. The first problem is single grains being "broken" into more than one piece. This problem is associated with noise in the data and/or the misidentification of grain centers (which in turn stems from either unusual grain shapes or limitations in the voxel resolution and resulting burn). The second problem is the opposite situation: the identification of a single large grain that should probably be broken into more than one piece (although this decision is subjective in consolidated materials). Both problems appear to be more pronounced for the current sandstone data compared to unconsolidated sands. Solutions to these problems are being implemented, but are not yet validated, and thus were not used in the current work.

Fortunately, the main problem with the current image appears to be the division of single grains into more than one piece, which will not affect the network generation process in a detrimental way; an increased number of grains will simply cause the algorithm to search for more pores. However, the final pore locations are determined by the optimization procedure and reflect local geometry regardless of whether the local grains were reconstructed in a reasonable way. Hence, the grain-based algorithm generates a physically representative network even if problems occur in the grain reconstruction process.

Table 5 contains selected parameters for the two different network generation techniques used on Sample A. **Fig. 6** shows histograms of the inscribed pore-size, inscribed pore-throat-size, and pore coordination number for the grain-based network. **Fig. 7** is a graphical representation of the two different network structures in a small interior section of the sandstone.

The most striking difference between the two networks is the number of pores, with the grain-based network having many fewer pores and thus longer pore throats spanning the gaps between the pores. This is a consequence of the logic in the grain-based algorithm, which uses the Delaunay tessellation of the grains as seed locations for potential pores. In contrast, the voxel-based algorithm searches for pores from each voxel location, which results in the identification of many more local extrema (i.e., locations of maximum inscribed spheres). Although the difference in pore numbers is large, it is still not possible to declare one network more correct than the other because discretization of the pore space is an arbitrary process (within reason of course). The key is that in both cases the network is a one-to-one mapping of the pore structure, and in both cases the pores are defined using the same rigorous definition: a local maximum in the distance function $d(x,y,z)$. The most effective illustration of these points is to examine the two

TABLE 5—QUANTITATIVE RESULTS FROM NETWORK MODELING OF THE SANDSTONE IMAGES

	Sandstone A		Sandstone B
	Grain-Based Network	Voxel-Based Network	Grain-Based Network
N_G	2,334		2,185
D_G (μm)	101		100
N_P	10,768	65,574	9,063
D_P (μm)	34	18	39
D_{PT} (μm)	31	26	38
L_{PT} (μm)	77	35	92.8
Z	3.21	3.16	3.15
ε	0.186	0.187	0.160
K_{xx} (mD)	410	430	1630
K_{yy} (mD)	530	570	850
K_{zz} (mD)	320	360	631

networks side by side, as in Fig. 7, and note that, despite differences in the details, the trends in network structure are the same (e.g., the appearance of large pores at the same locations; gaps in the network structure at the same locations, and so on).

The other notable point from the data presented here is the relatively small difference between the pore-throat diameters and the pore diameters, which is a consequence of the more tube-like pore structure that can occur in consolidated sands. In fact, in the voxel-based network, the average pore size is smaller than the average throat size. Although this is counter to the traditional pore and pore-throat model, it is a consequence of the high density of pores in the second network. The void space comprises strings of largely overlapping pores rather than distinct pores connected by long throats; the pore-throat diameter is simply the size of the channel at the point where two inscribed spheres overlap, and thus is not necessarily smaller than the adjacent pores.

Flow Modeling. The networks were used to model single-phase low-Reynolds-number flow of a Newtonian fluid. The flow modeling was performed after cropping 100 μm from all sides of the networks so as to avoid edge effects that are caused by the boundary of the volume data.

A pressure gradient was imposed in one of the coordinate directions and the resulting volumetric flowrate was computed. Permeability was then calculated using Darcy's law (see Table 5). This process was repeated for all three coordinate directions defined by the imaging volume. Note that K_{zz} does *not* imply orientation with respect to a bedding plane; because the sample was taken from a small cutting, no attempt was made to align the tomography image with the geologic strata.

The ability to obtain dimensional permeability values is a consequence of using physically representative networks. That is, the network is a map of a specific-sized region of the sandstone, which allows for the computation of dimensional volumetric flowrates and cross-sectional areas for flow. Additionally, because of the one-to-one mapping, the model has no adjustable or scaling parameters. [The pore-throat hydraulic conductivities are determined using the formulas originally developed for sphere packings (Thompson and Fogler 1997) and therefore are not treated as adjustable parameters.]

The similarity in permeabilities for the two different networks created from sandstone A may be surprising, considering the different network structures. However, this fact is again a consequence of using physically representative networks: in the network with fewer pores and pore throats, the throats are longer and therefore exhibit larger hydraulic resistance. Put simply, everything comes out in the wash.

Fig. 8 is a grayscale mapping of single-phase flow through the same region of sandstone A shown in Fig. 7b (the voxel-based network). The pressure gradient is from left to right for this simulation, and brighter shades indicate higher flowrates. This graphic shows clearly the heterogeneity in the flow pattern that results from the pore morphology, and demonstrates the conventional wisdom that relatively few pores carry a large fraction of the fluid. This graphic is also an effective illustration of the rationale for using network modeling, as opposed to simpler effective medium or bundle-of-tubes models. Although these simpler models may predict correct permeabilities given the proper pore statistics, they do not capture the flow heterogeneity that contributes strongly to processes such as solute dispersion.

Discussion

A grain-reconstruction algorithm (originally developed for unconsolidated sands) has been applied to consolidated sandstones. With additional development and testing, we believe that this algorithm can be used as a tool for quantitative analysis of the granular structure in sandstones. This paper uses a grain-reconstruction process as a template for generating a physically representative network model of the pore structure. The main advantages of this new approach are that the network is tied to a correct characteristic scale for the materials (i.e., the grain scale), the algorithm is more than an order of magnitude faster (compared to an equivalent voxel-based algorithm), and the resulting networks are less dependent on voxel resolution.

Future research should examine how different network structures (i.e., two different networks that are intended to represent the same material) affect the modeling of transport phenomena. To begin studying this issue, we ran the current algorithm in two ways: as a voxel-based algorithm and as a grain-based algorithm. These two approaches resulted in dramatically different network structures: the most obvious difference is in the number of pores, but this in turn affects most other parameters, including coordination number, throat length, and throat conductivity. Interestingly, despite the fact that the voxel-based network contained six times the number of pores, the average permeability difference (for the three directions) is only 7.5%. This result is encouraging because it means that the physically representative network generation process (which is free of adjustable parameters) is working as intended with respect to single-phase permeability. Nonetheless, we expect that multiphase simulations will be more sensitive to factors such as pore coordination number because current multiphase models rely more on rule-based algorithms compared to the single-phase models. This is a topic of ongoing research.

We conclude by commenting on the issue of image resolution. From our experience with grain-based modeling, we suggest a minimum of 10 VPD in order to extract reasonably good statistics for the solid-phase structure in unconsolidated materials (Thompson et al. 2006). However, this value (10 VPD) may need to be significantly higher for pore networks. Consider that when three spheres are placed in contact to form a pore throat (i.e., the ge-

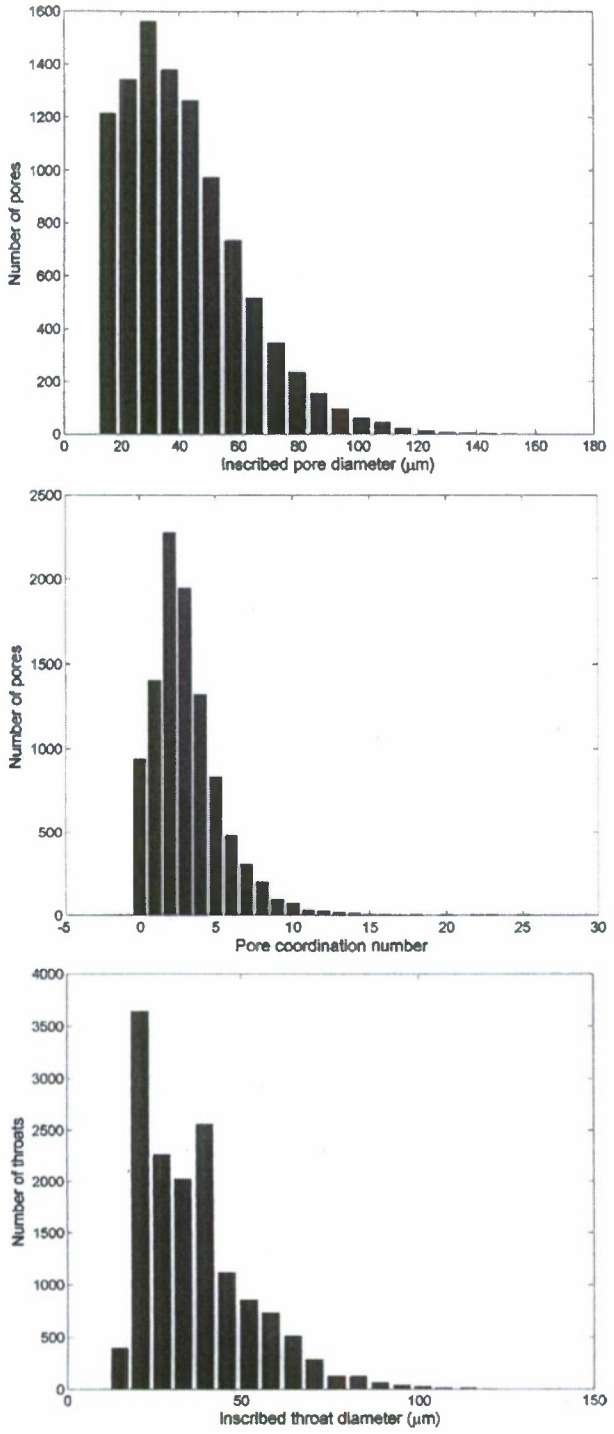

Fig. 6—Morphology of the pore space in sandstone A: (a) pore-size distribution (inscribed); (b) pore-coordination-number distribution; (c) pore-throat-size distribution (inscribed).

ometry in a rhombohedral packing), the inscribed diameter of the passage is equal to $0.155D_{sphere}$. Hence, a 10 VPD image will provide only 1–2 voxel resolution at a pore throat, which is the crucial area for flow modeling. This issue is exacerbated when a particle size distribution exists, or with consolidation. Table 3 from this paper provides a good starting point for assessing the errors in pore parameters that stem from voxel resolution issues.

Acknowledgments

The core samples were obtained in a study funded by the University of Texas at Dallas Quantitative Sedimentology Research Consortium funded by BP and Chevron, Geophysical Consortium and Center for Lithospheric Studies, and selected for analysis using funding from the US Department of Energy, contracts DOE/SC/15167-1 to LSU and DE-FG0301ER15166 to UTD. This material is based in part upon work supported by the National Science Foundation under Grant No. EAR-0207788 (CW) and ACS PRF grant 41169-AC 9 (CW). Use of the Advanced Photon Source was supported by the US Department of Energy, Office of Science, Office of Basic Energy Sciences, under Contract No. W-31-109-Eng-38. This research was conducted using high-performance computational resources provided by Louisiana State University (www.lsu.edu/hpc).

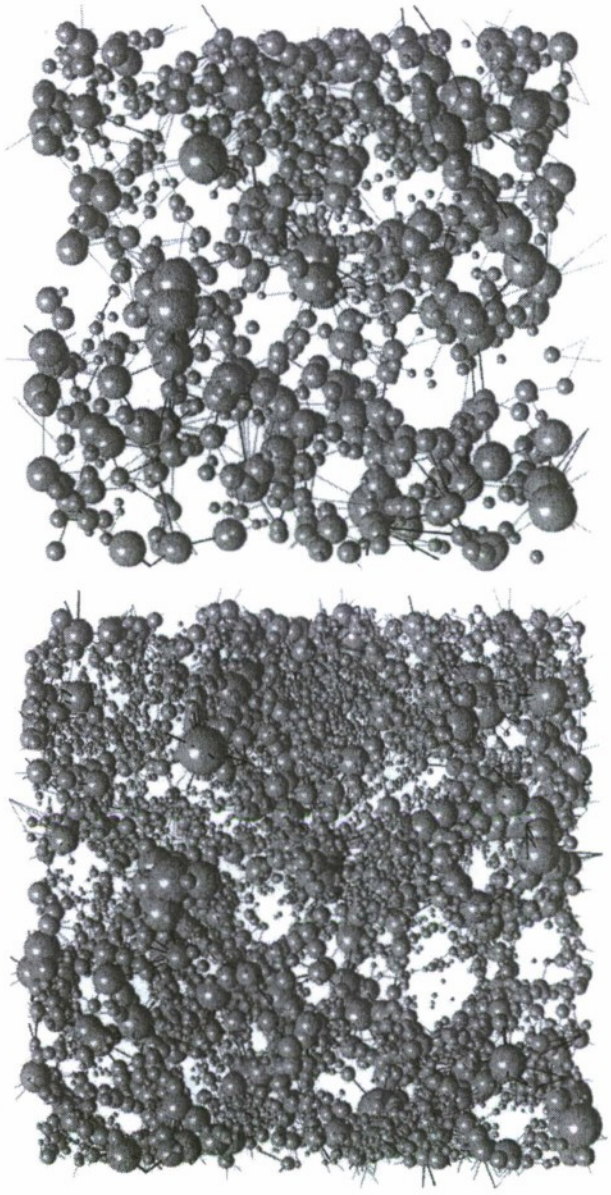

Fig. 7—Sections of two different networks generated from the same tomography image: (a) created using the grain-based algorithm; (b) created using the voxel-based algorithm.

References

Al-Raoush, R.I. and Willson, C.S. 2005a. A Pore-scale Investigation of a Multiphase Porous Media System. *J. Contam. Hydrology* **77** (1–2): 67–89. DOI: 10.1016/j.jconhyd.2004.12.001.

Al-Raoush, R.I., and Willson, C.S. 2005b. Extraction of physically realistic pore network properties from three-dimensional synchrotron X-ray mi-

Fig. 8—Representation of single-phase flow in a small section of the voxel-based network from the tidally-reworked sandstone (sample A).

crotomography images of unconsolidated porous media systems. *Journal of Hydrology* **300** (1–4): 44–64. DOI: 10.1016/J.Jhydrol.2004.05.005.

Al-Raoush, R.I., Thompson, K., and Willson, C.S. 2003. Comparison of network generation techniques for unconsolidated porous media. *Soil Sci. Soc. Am. J.* 67: 1687–1700.

Bakke, S. and Øren, P.E. 1997. 3-D Pore-Scale Modelling of Sandstones and Flow Simulations in the Pore Networks. *SPEJ* **2** (2): 136–149. SPE-35479-PA. DOI: 10.2118/35479-PA.

Balhoff, M.T. and Thompson, K.E. 2004. Modeling the steady flow of yield-stress fluids in packed beds. *AIChE J.* **50** (12): 3034–3048. DOI: 10.1002/aic.10234.

Bryant, S.L., King, P.R., and Mellor, D.W. 1993a. Network model evaluation of permeability and spatial correlation in a real random sphere packing. *Transport in Porous Media* 11 (1): 53–70. DOI: 10.1007/BF00614635.

Bryant, S.L., Mellor, D.W., and Cade, C.A. 1993b. Physically Representative Network Models of Transport in Porous Media. *AIChE J.* 39 (3): 387–396. DOI: 10.1002/aic.690390303.

Delerue, J.-F. and Perrier, E. 2002. DXSoil, a library for 3D image analysis in soil science. *Computers & Geosciences* 28 (9): 1041–1050. DOI: 10.1016/S0098-3004(02)00020-1.

Delerue, J.F., Perrier, E., Yu, Z.Y., and Velde, B. 1999. New algorithms in 3D image analysis and their application to the measurement of a spatialized pore size distribution in soils. *Phys. Chem. Earth A* **24** (7): 639–644. DOI: 10.1016/S1464-1895(99)00093-9.

Fatt, I. 1956. The Network Model of Porous Media: I. Capillary Pressure Characteristics. *Trans.*, AIME **207**: 144–159. SPE-574-G.

Finney, J.L. 1970. Random packings and the structure of simple liquids 1. The geometry of random close packing. *Proc. Roy. Soc. Lond. A* **319**: 479–493.

Gani, M.R. and Bhattacharya, J.P. 2003. Bed-scale facies architecture of an ancient delta lobe deposit of the Wall Creek Member, Central Wyoming, U.S.A. AAPG Annual Convention, Salt Lake City, Utah, 11–14 May.

Ioannidis, M.A., Kwiecien, M.J., Chatzis, I., MacDonald, I.F., and Dullien, F.A.L. 1997. Comprehensive Pore Structure Characterization Using 3D Computer Reconstruction and Stochastic Modeling. Paper SPE 38713 presented at the SPE Annual Technical Conference and Exhibition, San Antonio, Texas, 5–8 October.

Lee, K. et al. 2007. Three-dimensional facies architecture and three-dimensional calcite concretion distributions in a tide-influenced delta front, Wall Creek Member, Frontier Formation, Wyoming. *AAPG Bulletin* 91 (2): 191–214.

Liang, Z., Ioannidis, M.A., and Chatzis, I. 2000a. Geometric and topological analysis of three-dimensional porous media: Pore space partitioning based on morphological skeletonization. *J. Colloid Interface Sci.* 221 (1): 13–24. DOI: 10.1006/jcis.1999.6559.

Liang, Z., Ioannidis, M.A., and Chatzis, I. 2000b. Permeability and electrical conductivity of porous media from 3D stochastic replicas of the microstructure. *Chem. Eng. Sci.* 55 (22): 5247–5262. DOI: 10.1016/S0009-2509(00)00142-1.

Lindquist, W.B., Lee, S.-M., Coker, D.A., Jones, K.W., and Spanne, P. 1996. Medial axis analysis of void structure in three-dimensional tomographic images of porous media. *J. Geophys. Res.* **101** (B4): 8297–8310. DOI: 10.1029/95JB03039.

Lindquist, W.B., Venkatarangan, A., Dunsmuir, J., and Wong, T.-F. 2000. Pore and throat size distributions measured from synchrotron X-ray tomographic images of Fontainebleau sandstones. *J. Geophys. Res.* **105** (B9): 21509-21527. DOI: 10.1029/2000JB900208.

Lohman, G. 1998. *Volumetric Image Analysis*. New York City: John Wiley & Sons.

Lopez, X., Valvatne, P.H., and Blunt, M.J. 2003. Predictive network modeling of single-phase non-Newtonian flow in porous media. *J. Colloid Interface Sci.* **264** (1): 256–265. DOI: 10.1016/S0021-9797(03)00310-2.

Luchnikov, V.A., Medvedev, N.N., Oger, L., and Troadec, J.-P. 1999. Voronoi-Delaunay analysis of voids in systems of nonspherical particles. *Phys. Rev. E* 59 (6): 7205–7212. DOI: 10.1103/PhysRevE.59.7205.

Mellor, D.W. 1989. Random close packing (RCP) of equal spheres: structure and implications for use as a model porous medium. PhD thesis, Milton Keynes, U.K.: Open University.

Oh, W. and Lindquist, B. 1999. Image thresholding by indicator kriging. *IEEE Transactions on Pattern Analysis and Machine Intelligence* 21 (7): 590-602. DOI: 10.1109/34.777370.

Øren, P.-E., Bakke, S., and Arntzen, O.J. 1998. Extending Predictive Capabilities to Network Models. *SPEJ* **3** (4): 324–336. SPE-52052-PA. DOI: 10.2118/52052-PA.

Patzek, T.W. 2001. Verification of a Complete Pore Network Simulator of Drainage and Imbibition. *SPEJ* **6** (2): 144–156. SPE-71310-PA. DOI: 10.2118/71310-PA.

Press, W.H., Teukolsky, S.A., Vetterling, W.T., and Flannery, B.P. 1992. *Numerical Recipes in Fortran 77*. New York City: Cambridge University Press.

Reed, A.H. et al. 2005. Quantification of sediment properties and geoacoustic parameters from pore structure and grain contacts: A microcomputed tomography analyisis of SAX04 sands. *Proc.*, International Conference on Boundary Influences in High-Frequency, Shallow Water Acoustics, University of Bath, Bath, U.K., 5–9 September.

Scheidegger, A.E. 1974. *The Physics of Flow Through Porous Media*. Toronto, Ontario, Canada: University of Toronto Press.

Seright, R.S., Liang, J.-T., Lindquist, W.B., and Dunsmuir, J.H. 2002. Characterizing Disportation Permeability Reduction Using Synchrotron X-Ray Computed Tomography. *SPEREE* 5 (5): 355–364. SPE-79717-PA. DOI: 10.2118/79717-PA.

Seright, R.S., Liang, J.-T., Lindquist, W.B., and Dunsmuir, J.H. 2003. Use of X-ray computed microtomgraphy to understand why gels reduce relative permeability to water more than that to oil. *J. Pet. Sci. Eng.* 39 (3–4): 217–230. DOI: 10.1016/S0920-4105(03)00064-0.

Silin, D.B., Jin, G., and Patzek, T.W. 2003. Robust Determination of the Pore Space Morphology in Sedimentary Rocks. Paper SPE 84296 presented at the SPE Annual Technical Conference and Exhibition, Denver, 5–8 October. DOI: 10.2118/84296-MS.

Sok, R.M. et al. 2002. Direct and stochastic generation of network models from tomographic images; effect of topology on residual saturations. *Transport in Porous Media* **46** (2–3): 345–371. DOI: 10.1023/A:1015034924371.

Talukdar, M.S., Torsaeter, O., Ioannidis, M.A., and Howard, J.J. 2002. Stochastic reconstruction, 3D characterization and network modeling of chalk. *J. Pet. Sci. Tech.* 35 (1-2): 1–21. DOI: 10.1016/S0920-4105(02)00160-2.

Thompson, K.E. 2002. Fast and robust Delaunay tessellation in periodic domains. *Int. J. Numer. Meths. Eng.* 55 (11): 1345–1366. DOI: 10.1002/nme.558.

Thompson, K.E. and Fogler, H.S. 1997. Modeling Flow in Disordered Packed Beds from Pore-Scale Fluid Mechanics. *AIChE J.* **43** (6): 1377–1389. DOI: 10.1002/aic.690430602.

Thompson, K.E., Willson, C.S., and Zhang, W. 2006. Quantitative computer reconstruction of particulate materials from microtomography images. *Powder Technology* **163** (3): 169–182. DOI: 10.1016/j.powtec.2005.12.016.

Valvatne, P.H. and Blunt, M.J. 2003. Predictive Pore-Scale Network Modeling. Paper SPE 84550 presented at the SPE Annual Technical Conference and Exhibition, Denver, 5–8 October. DOI: 10.2118/84550-MS.

Karsten E. Thompson is an associate professor of chemical engineering at Louisiana State University. His research interests include computational modeling of porous materials. He holds a BS degree from the University of Colorado and MS and PhD degrees from the University of Michigan, all in chemical engineering. **Clinton S. Willson** is an associate professor in the Department of Civil and Environmental Engineering at Louisiana State University. His research interests include high-resolution, 3D imaging of multiphase flow in porous media. He holds a BS degree in aerospace engineering from Pennsylvania State University, as well as an MS degree in environmental health engineering and a PhD degree in civil engineering, both from the University of Texas at Austin. **Christopher D. White** has been on the faculty of the Department of Petroleum Engineering at Louisiana State University since 1999. He formerly worked at Shell Development Company and the Bureau of Economic Geology. His interests include reservoir geomodeling and engineering. White holds a BS degree from the University of Oklahoma as well as MS and PhD degrees from Stanford University, all in petroleum engineering. **Stephanie L. Nyman** is a PhD candidate and Assistant Lecturer at the University of Waikato, Hamilton, New Zealand. Her geologic specialty is clastic diagenesis, with a research interest in carbonate cement within subsurface hydrocarbon seep systems. She holds an MSc degree from the University of Texas at Dallas. **Janok P. Bhattacharya** is the Robert E. Sheriff Professor of Sequence Stratigraphy in the Department of Earth and Atmospheric Sciences at the University of Houston. Following a Natural Sciences and Engineering Research Council post-doc at the Alberta Geological Survey in Edmonton, Janok worked for the Bureau of Economic Geology in Austin; ARCO Research in Plano, Texas; and the University of Texas at Dallas before joining the University of Houston. His research interests include deltaic sedimentology and sequence stratigraphy, the local control of structure on stratigraphy, and reservoir architecture of clastic depositional systems. He has authored or co-authored approximately 50 technical papers and over 100 abstracts. He holds a BSc degree from Memorial University of Newfoundland, Canada, and a PhD degree from McMaster University, Hamilton, Ontario, Canada. **Allen H. Reed** is a geologist with the Naval Research Laboratory. His research interests are in marine sedimentology, including microfocus-computed tomography and image analysis of porous media, and the influence of muddy sediments on dissipation of wave energy. He holds a BS degree in oceanography from Humboldt State University, an MS degree in marine sciences from the University of Southern Mississippi, and a PhD degree in oceanography and coastal studies from Louisiana State University.